

Ultracool Dwarfs Observed with the Spitzer Infrared Spectrograph - III. Dust Grains in Young L Dwarf Atmospheres Are Heavier

Genaro Suárez,^{1,2}★ Stanimir Metchev,^{2,3}

¹*Department of Astrophysics, American Museum of Natural History, Central Park West at 79th St, New York, NY, 10024, USA*

²*Department of Physics and Astronomy, The University of Western Ontario, 1151 Richmond St, London, Ontario, N6A 3K7, Canada*

³*Institute for Earth and Space Exploration, The University of Western Ontario, 1151 Richmond St, London, Ontario, N6A 3K7, Canada*

Accepted XXX. Received YYY; in original form ZZZ

ABSTRACT

Analysis of all archival 5–14 micron spectra of field ultracool dwarfs from the Infrared Spectrograph on the Spitzer Space Telescope has shown that absorption by silicates in the 8–11 micron region is seen in most L-type (1300 K to 2200 K) dwarfs. The absorption is caused by silicate-rich clouds in the atmospheres of L dwarfs and is strongest at L4–L6 spectral types. Herein we compare averages of the mid-infrared silicate absorption signatures of L3–L7 dwarfs that have low ($\lesssim 10^{4.5}$ cm s⁻²) vs. high ($\gtrsim 10^5$ cm s⁻²) surface gravity. We find that the silicate absorption feature is sensitive to surface gravity and indicates a difference in grain size and composition between dust condensates in young and old mid-L dwarfs. The mean silicate absorption profile of low-gravity mid-L dwarfs matches expectations for ~ 1 micron-sized amorphous iron- and magnesium-bearing pyroxene ($\text{Mg}_x\text{Fe}_{1-x}\text{SiO}_3$) grains. High-gravity mid-L dwarfs have silicate absorption better represented by smaller ($\lesssim 0.1$ μm) and more volatile amorphous enstatite (MgSiO_3) or SiO grains. This is the first direct spectroscopic evidence for gravity-dependent sedimentation of dust condensates in ultracool atmospheres. It confirms theoretical expectations for lower sedimentation efficiencies in low-gravity atmospheres and independently confirms their increased dustiness.

Key words: brown dwarfs — stars: atmospheres — infrared: stars

1 INTRODUCTION

The atmospheres of L spectral type dwarfs have effective temperatures between approximately 1300–2200 K (Kirkpatrick 2005; Filippazzo et al. 2015). It is observationally established, based both on their very red optical to near-infrared colours (Knapp et al. 2004; Kirkpatrick 2005) and on the direct detection of silicates in mid-infrared spectra (Roellig et al. 2004; Cushing et al. 2006;Looper et al. 2008; Suárez & Metchev 2022), that these atmospheres are dusty. Theoretically, silicon-bearing molecules such as quartz (SiO_2), pyroxene ($\text{Mg}_x\text{Fe}_{1-x}\text{SiO}_3$), and olivine ($\text{Mg}_x\text{Fe}_{2-x}\text{SiO}_4$), including the Mg-rich endmembers enstatite (MgSiO_3) and forsterite (Mg_2SiO_4), are expected to start forming 0.1–1 μm -sized silicate dust condensates at ≤ 2000 K (Burrows et al. 1997, 2001; Ackerman & Marley 2001; Lodders 2002). The theory dictates that the silicate condensate clouds sediment to deeper levels as the L-type substellar atmosphere cools, and at $\lesssim 1300$ K effective temperatures the clouds drop below the altitude of the ~ 0.1 bar pressure level of the mid-infrared photosphere (Luna & Morley 2021). The onset of dust cloud formation at warm temperatures and their later sedimentation at cooler temperatures have been observationally confirmed from 5–14 μm mid-infrared spectra of L dwarfs (Suárez & Metchev 2022).

In addition to being dependent on temperature, dust sedimentation in the atmosphere is also a function of surface gravity. Cloud settling

is less efficient at lower gravity, which should lead to increased cloud vertical depth and optically thicker cloud decks (Stephens et al. 2009; Madhusudhan et al. 2011; Marley et al. 2012; Charnay et al. 2018). Indeed, unusually red optical/near-infrared colours are a well-known trait of young L dwarfs (e.g., Kirkpatrick et al. 2006, 2008; Looper et al. 2008; Faherty et al. 2016), which have lower surface gravity because of their larger radii at their earlier evolutionary stages (e.g., Burrows et al. 1997). Indirect evidence of the greater importance of dust in younger L-type atmospheres also comes from their enhanced brightness variations (Metchev et al. 2015; Biller et al. 2015; Vos et al. 2018, 2019; Bowler et al. 2020), understood to be caused by the rotationally modulated visibility of large dust cloud features (Burgasser et al. 2002; Artigau et al. 2009).

The role of gravity in sedimentation also dictates that heavier dust grains, made of potentially more refractory compounds, should sediment first, leaving lighter grains at higher altitudes (Ackerman & Marley 2001; Cooper et al. 2003). However, this has yet to be observationally demonstrated, and is the main finding of the present study.

The physical properties and mineral composition of silicate dust in brown dwarf atmospheres remain relatively unexplored. They require a population analysis of high signal-to-noise ratio (SNR) mid-infrared spectra of these objects that awaits observations with the James Webb Space Telescope (JWST). To date, only a limited sample has been analysed based on low-resolution spectra with the Spitzer Space Telescope Infrared Spectrograph (IRS; Houck et al. 2004), and only during Spitzer’s 2003–2009 Cryogenic Mission. Namely,

★ E-mail: gsuares@amnh.org

theoretical modelling to match six moderate- to high-SNR L dwarf Spitzer IRS spectra (Roellig et al. 2004; Cushing et al. 2006; Looper et al. 2008) has shown that dust clouds in L dwarfs comprise a combination of amorphous silicates (quartz, enstatite, and forsterite) and iron condensed in $\leq 1 \mu\text{m}$ -sized grains (Cushing et al. 2006; Burningham et al. 2021; Luna & Morley 2021). For over a decade, this small sample of L dwarf spectra has been the only source to probe cloud chemistry directly. Recently, silicate absorption was also detected in the atmosphere of the late-L planetary-mass companion VHS J125601.92–125723.9 b using JWST Mid-Infrared Instrument (MIRI) spectra (Miles et al. 2022) and forsterite clouds have been inferred in the IRS spectra of two young (~ 200 Myr) early-T dwarf atmospheres (Vos et al. 2022a).

The study of Suárez & Metchev (2022) re-assessed all 113 Spitzer IRS observations of $\geq M5$ ($T_{\text{eff}} \leq 3000$ K) dwarfs outside of known ≤ 10 Myr-old star-forming regions. A comparative analysis of the 69 L dwarf spectra in the sample established many more instances of spectroscopic silicate cloud detections beyond the six known prior. The study revealed that silicate clouds first form, then thicken, and sediment out of the visible atmosphere as the effective temperature decreases from ≈ 2000 K to ≈ 1300 K. While the Suárez & Metchev (2022) analysis focused mostly on ≥ 500 Myr-old field dwarfs outside of known star-forming regions, it also included four L3–L6.5-type dwarfs with spectroscopic and kinematic evidence of youth (few tens of Myr). This sample of relatively young objects, complemented with old counterparts, allows an investigation of the surface gravity (or age) dependence of silicate absorption in ultracool atmospheres.

Herein we compare the silicate absorption in the mid-infrared Spitzer IRS spectra of young, low-surface gravity mid-L dwarfs ($\log g \lesssim 4.5$; $1800 \text{ K} \gtrsim T_{\text{eff}} \gtrsim 1200 \text{ K}$) to their older, higher-gravity ($\log g \gtrsim 5.0$) counterparts in the Spitzer IRS sample. Our analysis confirms the theoretical expectations of gravity-dependent sedimentation of dust clouds from Ackerman & Marley (2001); Cooper et al. (2003). Specifically, we find that heavier dust grains have higher abundances in lower-gravity L-type atmospheres than they do at higher surface gravity. In Section 2 we describe the sample and the approach followed to compare silicate absorption profiles in young and old ultracool atmospheres. An investigation of how the silicate absorption depends on surface gravity is presented in Section 3. In Section 4 we compare observed silicate absorption profiles to theoretical expectations. We summarise our conclusions in Section 5.

2 SAMPLE AND METHODS

To assess the surface gravity dependence of the silicate absorption feature we define sub-samples of young and old mid-L dwarfs with the strongest silicate features. We then use a separate sub-sample of mid-L dwarfs with no discernible silicate features to estimate the continuum for the silicate-rich spectra. Table 1 lists the L3–L7 dwarfs in each sub-sample and their relevant properties.

2.1 Selection of Mid-L Dwarfs with Silicate-rich and Silicate-poor Spectra

To measure silicate absorption strengths we iterated on Suárez & Metchev (2022), and defined a silicate index as the ratio of an interpolated continuum to the median flux at $9.3 \mu\text{m}$ in a $0.6 \mu\text{m}$ -wide window. The interpolated continuum was calculated as the best $\log F_{\nu}$ vs. $\log \lambda$ linear fit to the fluxes in two regions that frame the silicate feature and are mostly free of other molecular absorption: $7.2\text{--}7.7 \mu\text{m}$ and $13.0\text{--}14.0 \mu\text{m}$ (Figure 1). We changed the central

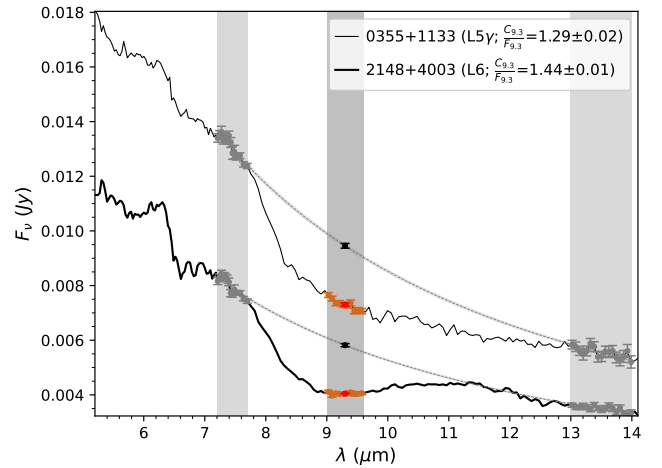


Figure 1. Silicate index measurements for the low-surface gravity ($\log g = 4.45 \pm 0.21$; Filippazzo et al. 2015) L5 γ dwarf 2MASS J03552337+1133437 (top spectrum) and the high-surface gravity ($\log g = 5.13 \pm 0.28$; Filippazzo et al. 2015) L6 dwarf 2MASS J21481628+4003593 (bottom spectrum). The silicate index is defined as the ratio of the interpolated continuum (black point; $C_{9.3}$) to the median flux (red point; $F_{9.3}$) at $9.3 \mu\text{m}$ in a $0.6 \mu\text{m}$ -wide window (brown points in the central dark grey vertical region). The interpolated continuum (black dashed curve with uncertainties shown by the grey shaded region) is obtained as a linear $\log F_{\nu}$ vs. $\log \lambda$ fit to the fluxes in the $7.2\text{--}7.7 \mu\text{m}$ and $13\text{--}14 \mu\text{m}$ continuum regions (grey points in the outer light grey vertical regions). The $C_{9.3}/F_{9.3}$ silicate index is indicated in the legend.

wavelength of the silicate absorption index (to $9.3 \mu\text{m}$ from $9.0 \mu\text{m}$) compared to Suárez & Metchev (2022) to better match theoretical expectations from Luna & Morley (2021). The long-wavelength continuum region was further moved to $13.0\text{--}14.0 \mu\text{m}$ vs. $11.2\text{--}11.8 \mu\text{m}$ to exclude as much as possible of the red wing of the silicate feature for both young and old dwarfs (Figure 1).

Figure 2a shows the updated silicate index measurements as a function of spectral type for the M5–T8 dwarfs in Suárez & Metchev (2022). We adopt optical spectral types for M and L dwarfs and infrared types for T dwarfs. The dashed line traces the median silicate index value in two spectral subtype-wide bins. As observed in Suárez & Metchev (2022), the L dwarfs show a systematic excess in silicate index values above a declining trend from late-M to T dwarfs. This indicates near-ubiquitous $8\text{--}11 \mu\text{m}$ silicate absorption in L dwarfs. The updated definition of the silicate index with a redder central wavelength and a wider continuum span compared to Suárez & Metchev (2022) shows that silicate absorption is already detectable in the average L1 dwarf, slightly earlier than the L2 onset noted in Suárez & Metchev (2022).

We define a silicate index excess (ΔSi) for each ultracool dwarf as the difference between its measured silicate index and the median index for its spectral type (black dashed curve in Figure 2a). Figure 2b shows the silicate excess as a function of spectral type for the full sample in Suárez & Metchev (2022). We constrain our analysis to L3–L7 dwarfs, as they have the strongest absorption on average, and their $8\text{--}11 \mu\text{m}$ silicate absorption is not contaminated by the $7\text{--}9 \mu\text{m}$ methane absorption that sets in at spectral type L8 (Suárez & Metchev 2022). From all L3–L7 dwarfs, we select those with $\Delta\text{Si} > 0.10$ and for which ΔSi is positive by more than twice its uncertainty (i.e., $\text{SNR}(\Delta\text{Si}) > 2$) as mid-L dwarfs with silicate-rich spectra. This selection includes three of the five mid-L dwarfs

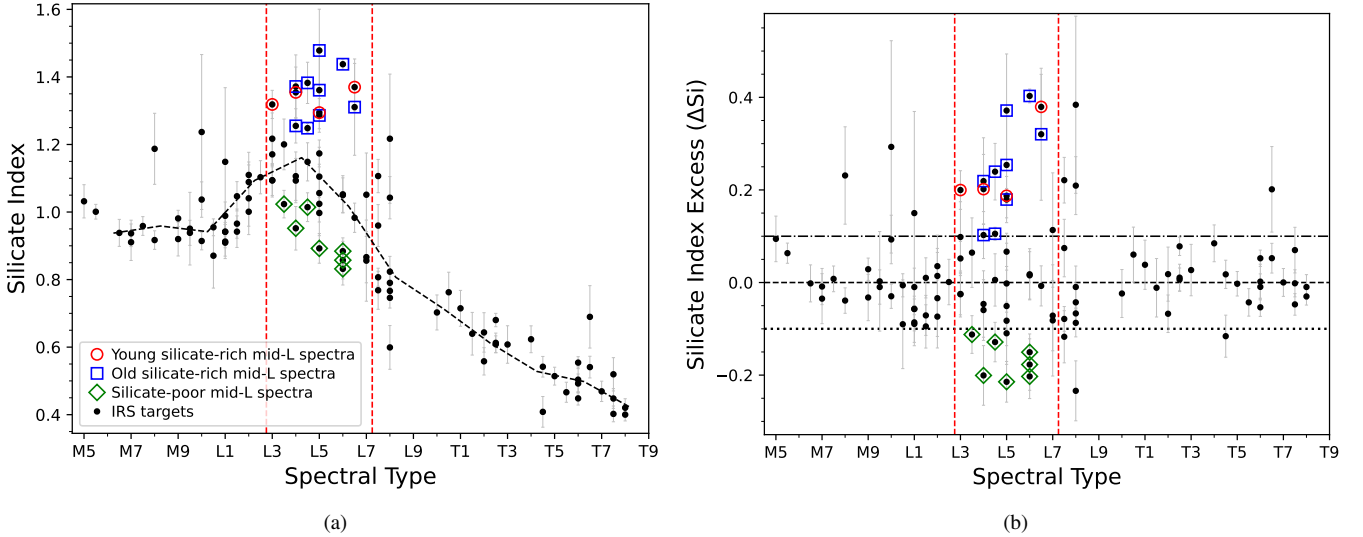


Figure 2. (a): Silicate index as a function of spectral type for all 113 M5–T9 dwarfs with IRS spectra (black points) in Suárez & Metchev (2022). The black dashed curve corresponds to the median silicate index in bins of two spectral subtypes. The vertical red dashed lines delimit the L3–L7 spectral type range (slightly shifted for clarity) within which we analyse young objects with silicate-rich spectra (red circles), old objects with silicate-rich spectra (blue squares), and objects with silicate-poor spectra (green diamonds). **(b):** Silicate index excess (ΔSi), defined as the difference between the measured and the median (black dashed line) silicate index for each object (Section 2.1). $\Delta Si > 0.10$ (above the black dash-dotted line) and $\Delta Si < -0.10$ (below the black dotted line) were used to select silicate-rich and silicate-poor spectra. The rest of the symbols are the same as in (a).

previously known or suspected to have silicate absorption: 2MASS J18212815+1414010 (L4.5), 2MASS J21481633+4003594 (L6), and 2MASS J22244381–0158521 (L4.5; Cushing et al. 2006; Looper et al. 2008). The remaining two—2MASS J00361617+1821104 (L3.5) and 2MASS J15074769–1627386 (L5; Cushing et al. 2006)—have silicate indices closer to the median silicate index for their spectral subtypes. That is, they still likely have silicate absorption, but it does not stand out in strength compared to other L dwarfs of similar spectral types. (The sixth L dwarf with previously reported silicate absorption is 2MASS J02550357–4700509 (L8; Roellig et al. 2004), which is outside of the L3–L7 spectral type range considered here.)

We select seven objects in the L3–L7 range with the most negative silicate excess as a sub-sample representative of mid-L dwarfs with silicate-poor spectra. Mirroring the selection of silicate-rich spectra, we select these to have $\Delta Si < -0.10$ and a ΔSi value that is negative by more than twice its uncertainty. It is highly likely that the atmospheres of the mid-L dwarfs with silicate-poor spectra are still abundant in silicates. However, the silicate condensates may have mostly settled to a layer below the visible 8–11 μm photosphere. Hence, their spectra are representative of the expected mid-infrared continuum and absorption by other non-silicate species, such as water and methane.

2.2 Assignment of Surface Gravity

We use spectral features known to be associated with gravity, corroborated with kinematic association, or lack thereof, to known young stellar moving groups to assign mid-L dwarfs into categories of low-versus high-surface gravity. We disfavour surface gravity determinations from photospheric model fits to the low-resolution Spitzer IRS spectra themselves, or to broad spectral energy distributions (SEDs) that are not constrained by age. Gravity determinations from Spitzer IRS spectra do not conform well with results from near-infrared spectra that contain pressure-sensitive lines or features (e.g., Suárez et al. 2021). Broad SEDs are excellent for bolometric luminosity es-

timates, but are poor for determining surface gravities (Cushing et al. 2008). They benefit from an evolutionary model-dependent radius or mass estimate for improved effective temperature and surface gravity determination (e.g., Cushing et al. 2008; Filippazzo et al. 2015).

There are four L3–L6.5 dwarfs among the 13 silicate-rich spectra with a γ spectroscopic designation indicative of low surface gravity and hence youth. We extract these as a sub-sample of young silicate-rich mid-L spectra. The remaining nine (L4–L6.5) dwarfs with silicate-rich spectra have no previously published spectroscopic indications of youth. We assign these to the sub-sample of old silicate-rich mid-L spectra. We verify the age classification of our mid-L dwarfs with silicate-rich spectra by checking whether any of them may be kinematically associated with known nearby young stellar moving groups. Three of the γ -classified objects (2MASS J03552337+1133437, 2MASS J14252798–3650229, and 2MASS J22443167+2043433) are bona fide members of the 110–150 Myr-old (Luhman et al. 2005; Barenfeld et al. 2013) AB Doradus moving group (Liu et al. 2013; Gagné et al. 2015; Vos et al. 2018) and 2MASS J05012406–0010452 is a possible member of the Columba or Carina moving groups (Gagné et al. 2015), which are coeval at 20–40 Myr (Torres et al. 2008). Conversely, the BANYAN Σ algorithm (Gagné et al. 2018) tool indicates that seven of the nine old silicate-rich mid-L dwarfs have a >96% probability of being field objects. Only 2MASS J17534518–6559559 (L4) and 2MASS J09201223+3517429 (L6.5) have 85% and 14% probabilities of membership in the 40–50 Myr-old (Zuckerman 2019) Argus and 110–150 Myr AB Doradus moving groups, respectively. However, kinematic association with a young stellar moving group is not a sufficient indicator of youth. Because of the lack of spectroscopic confirmation of low surface gravity, we keep these two objects in our sample of old mid-Ls. Their IRS spectra have low-SNR (≈ 10 at 9 μm), and so do not significantly contribute to our representation of old silicate-rich mid-L dwarfs (Section 2.4).

The above division in low vs. high surface gravity sub-samples is mostly consistent with surface gravity determinations for the individual objects in the published literature. The four young dwarfs all have

$\log g \lesssim 4.5$ ($g \lesssim 10^{4.5} \text{ cm s}^{-2}$) from combined constraints on their bolometric luminosities from trigonometric parallaxes and (photospheric model fits to) SEDs, and on the ages for the respective parent associations (Filippazzo et al. 2015; Gagné et al. 2015; Vos et al. 2018). The old dwarfs with gravity estimates all have $\log g \gtrsim 5.0$ ($g \gtrsim 10^{5.0} \text{ cm s}^{-2}$) (Cushing et al. 2008; Gagné et al. 2015; Filippazzo et al. 2015; Dupuy & Liu 2017; Luna & Morley 2021; Burningham et al. 2021). Some studies point to higher $\log g$ values for two of the four young dwarfs (2MASS J22443167+2043433 in Stephens et al. 2009; 2MASS J14252798–3650229 in Gagné et al. 2015), or to a lower $\log g$ for one of the old dwarfs (2MASS J22244381–0158521; Cushing et al. 2008; Stephens et al. 2009). All of the discrepant gravities were obtained by fitting atmospheric models to broad SEDs without an age constraint, and so are potentially less accurate. For instance, while Gagné et al. (2015) find a field-like $\log g = 5.0 \pm 0.5$ for 2MASS J14252798–3650229 from an age-unconstrained photospheric model to the SED, they also note that this object is a young γ -class L4 dwarf from analysis of narrower spectral regions sensitive to surface gravity. Similarly, Cushing et al. (2008) and Stephens et al. (2009) find a relatively low $\log g = 4.5 \pm 0.5$ from age-unconstrained photospheric model fits to the SED of 2MASS J22244381–0158521. However, when combined with an evolutionary model appropriate for its otherwise field-age kinematics, the photospheric fit to the SED results in a higher surface gravity ($\log g \gtrsim 5.2$; Cushing et al. 2008; Filippazzo et al. 2015).

Figure 2 highlights the selected sub-samples of mid-L dwarfs from Table 1 according to their silicate strength and surface gravity.

2.3 Continuum Removal

Figure 3a illustrates the difference in the silicate absorption feature between the selected sub-samples of silicate-poor and silicate-rich mid-L spectra. The full 5.2–14.2 μm spectra are shown scaled to the same average flux in the 7.2–7.7 μm and 13.0–14.0 μm continuum regions. The weighted average of the silicate-poor mid-L spectra (black curve), obtained using the inverse squared values of the errors on the scaled flux as weights, traces the mid-infrared continuum in the near-total absence of silicate absorption. It does not exhibit a significant scatter and is well-represented by a second-order polynomial fit (black dashed curve) between 7.2–14.0 μm . The silicate-rich spectra exhibit characteristic broad absorption from 8 μm out to 11–13 μm .

To isolate the silicate absorption signature in silicate-rich mid-L dwarfs from that of other potential continuum absorbers, we divide all normalised IRS spectra by the quadratic fit to the weighted average silicate-poor mid-L continuum. The continuum-divided mid-L spectra are shown in Figure 3b, where we have narrowed the rendering to the 7.2–14.0 μm range that spans the ~ 8 –13 μm silicate absorption. The underlying assumption for the continuum removal is that any non-silicate absorbers (such as water or methane) are present at similar strength in the silicate-poor and silicate-rich mid-L spectra. While that appears to mostly be the case, given the similarity among the continuum-divided mid-L spectra outside the silicate absorption region (Figure 3b), there remain some systematic differences. Namely, the spectra of mid-L dwarfs with enhanced silicate absorption generally have higher fluxes at $< 7.5 \mu\text{m}$ and lower fluxes at $\gtrsim 13 \mu\text{m}$ compared to the silicate-poor spectra. The culprit for the short-wavelength difference is likely water absorption. Mid-L dwarfs with higher silicate content in the upper atmosphere likely have some of the gas-phase water column blocked, and hence exhibit weaker water absorption. At long wavelengths the culprit is likely silicates themselves. The absorption signatures of the nine-micron

amorphous pyroxene (including enstatite) features may extend beyond 13 μm (Luna & Morley 2021).

Despite the systematics at the edges, the continuum-divided silicate-rich spectra do isolate the main part of the silicate feature well. A difference in the red wing of this feature is discernible in Figure 3b between the young (brown) and old (orange) silicate-rich mid-L spectra, with the young mid-L spectra consistently tracking below the old spectra at $> 10 \mu\text{m}$. However, most of the individual spectra are too noisy to assess this difference. We proceed by scaling and averaging the silicate absorption profiles themselves.

2.4 Scaling and Averaging of Silicate Absorption Profiles

With the continua of the silicate-rich spectra factored out, we scale the strengths of the silicate absorption profiles to each other to account for differences in the silicate column density among objects. We use the flux median of the silicate-rich spectra within a 0.6 μm -wide region centred on 9.3 μm (Cushing et al. 2006; Luna & Morley 2021) to scale all absorption profiles to the same depth (Figure 4a). We can apply such scaling without fear of contamination from non-silicate absorbers, because we have already removed their effect after dividing by the silicate-poor continuum. In so far as the silicate species are similar among the different mid-L dwarfs, their normalised absorption profiles will also be similar as a function of wavelength, save for a multiplicative constant. However, small departures from similarities, as expected among different amorphous sub-types of silicates, are enhanced.

We take the weighted average of the scaled spectra for each of the sub-samples and obtain population-averaged silicate absorption profiles for young and old mid-L spectra. As for the combination of the silicate-poor spectra (Section 2.3), we use the inverse squared values of the errors on the scaled flux as weights. The combined spectra are shown in Figure 4a by red and blue curves, with correspondingly shaded one-sigma uncertainty regions. Figure 4a also includes the weighted average for continuum-divided silicate-poor mid-L spectra (in black) as an estimate of the accuracy of the continuum removal process. Because the continuum in the silicate absorption region was determined from the silicate-poor spectra, the continuum-divided weighted average of the silicate-poor spectra scatters around unity.

3 RESULTS: GRAVITY-DEPENDENT SILICATE ABSORPTION

Figure 4a shows that young silicate-rich mid-L spectra have a distinct absorption profile compared to old silicate-rich mid-L spectra. We observe three main differences.

1. Silicate absorption strength peaks at a 0.4 μm longer wavelength in young mid-L dwarfs. While the silicate absorption profiles for both the young and the old silicate-rich mid-L subsets were normalised to the same flux at 9.3 μm , Figure 4a shows that the central wavelengths at which each of the profiles is the deepest are different. We estimate these central wavelengths by fitting a third-order polynomial to each continuum-divided weighted-average silicate-rich spectrum over the 8.0–11.5 μm wavelength range. We find that silicate absorption peaks at $9.5 \pm 0.1 \mu\text{m}$ in young silicate-rich mid-L spectra and at $9.1 \pm 0.1 \mu\text{m}$ in old silicate-rich mid-L spectra, as shown by the red vertical dashed line and the blue vertical dotted line in Figure 4a. We estimate the central wavelength uncertainties from 10^4 Monte Carlo realizations of each scaled and averaged spectrum. We consider the flux at each wavelength as a Gaussian random variate centred on the weighted average flux, and a standard deviation

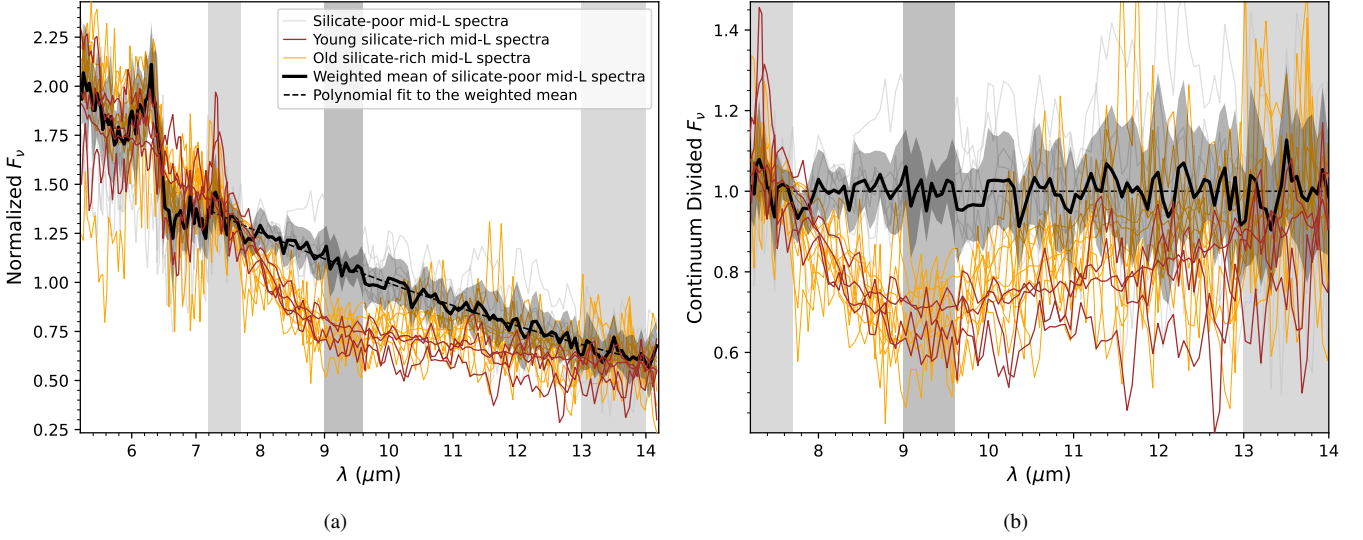


Figure 3. (a): Normalised comparison of four young silicate-rich (brown curves), seven old silicate-rich (orange curves), and seven silicate-poor (grey curves) L3–L6.5 spectra. The normalisation was performed to the median flux in the 7.2–7.7 μm and 13.0–14.0 μm continuum windows (light grey vertical regions) that surround the silicate absorption. The 9.0–9.6 μm window (medium grey vertical region) denotes the range where silicate absorption is on average the strongest. The weighted average of the silicate-poor spectra is indicated by the black curve and its uncertainty by the surrounding dark grey shaded region. The best second-order polynomial fit to this combined spectrum in the 7.2–14.0 μm range is represented by the black dashed curve. **(b):** The 7.2–14.0 μm sub-range of the same spectra as in (a), divided by the polynomial fit to the average silicate-poor mid-L continuum. By construction, the continuum-divided weighted average (black curve) of silicate-poor spectra scatters around unity (dashed line; same as in (a)).

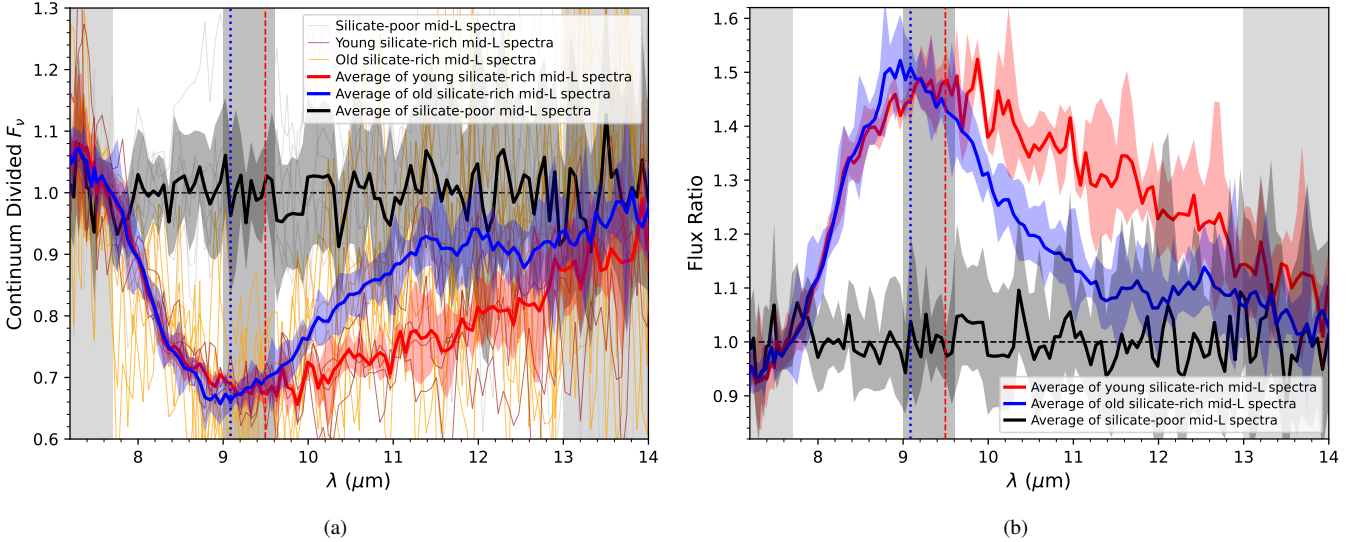


Figure 4. (a) Continuum-divided 7.2–14.0 μm subsections of the mid-L dwarf IRS spectra from Figure 3b with the strength of the silicate absorption in silicate-rich spectra scaled to the same median flux in a 0.6 μm -wide window centred on 9.3 μm (vertical grey band). Weighted averages of these mid-L spectra are shown as follows: young silicate-rich spectra (red), old silicate-rich spectra (blue), silicate-poor spectra (black). The uncertainties of the weighted-average spectra are shown by shaded regions of the corresponding colour. The vertical red dashed and blue dotted lines mark the wavelengths of strongest silicate absorption in young and old silicate-rich mid-L spectra, respectively (see Section 2.4). Spectra of individual objects follow the same colour scheme as in Figure 3. **(b)** Inverse of fluxes in panel (a). This representation allows a direct comparison with flux ratio predictions for condensate cloud vs. grey cloud models in Figure 7 of Luna & Morley (2021).

equal to the flux uncertainty. The central wavelength was measured in each realisation as explained above. The quoted uncertainty on the central wavelength is the 68% confidence interval on the central wavelengths from the Monte Carlo simulation.

2. Silicate absorption in young mid-L dwarfs is nearly twice

as broad. When scaled to the same absorption depth at 9.3 μm , the equivalent width of the silicate absorption in young mid-L dwarfs is $1.0 \pm 0.1 \mu\text{m}$, whereas for the old mid-L dwarfs it is $0.6 \pm 0.1 \mu\text{m}$. We estimate the uncertainties on the equivalent widths from the same Monte Carlo simulation used for the uncertainties on the central

wavelengths of the silicate absorption above. The absorption feature in young mid-L dwarfs spans almost the entire plotted range in Figure 4a, from $\sim 7.5 \mu\text{m}$ to $>13.0 \mu\text{m}$. In old mid-L dwarfs the silicate absorption strength tapers off beyond $\approx 11.5 \mu\text{m}$. Low-level silicate absorption in old mid-L dwarfs may still be present at $>11.5 \mu\text{m}$, as in young mid-L dwarfs. However, even in our weighted-averaged spectra the difference from the silicate-poor $11.5\text{--}13.0 \mu\text{m}$ continuum is marginal.

3. Silicate absorption in young mid-L dwarfs is more asymmetric towards longer wavelengths. Young mid-L dwarfs with silicate-rich spectra have a flatter silicate absorption profile for wavelengths longer than the feature peak compared to a sharper absorption profile in old mid-L dwarfs with silicate-rich spectra. The difference is most pronounced in the $10\text{--}12 \mu\text{m}$ wavelength range, where the scaled and averaged silicate absorption profile in young mid-L dwarfs is significantly stronger than in old mid-L dwarfs. Conversely, over $7.5\text{--}9.0 \mu\text{m}$ the absorption profiles are fully consistent with each other.

Overall, the silicate absorption profile in young ($\sim 20\text{--}150$ Myr; $\log g \lesssim 4.5$) silicate-rich mid-L spectra is redder, broader, and more asymmetric than in old ($\gtrsim 500$ Myr; $\log g \gtrsim 5.0$) silicate-rich mid-L spectra. This constitutes the first observational evidence for a surface gravity dependence of the mid-infrared silicate absorption in ultracool dwarf spectra.

4 DISCUSSION

Prior to Suárez & Metchev (2022), the existing Spitzer IRS spectra of the six L dwarfs inferred to show silicate absorption (Roellig et al. 2004; Cushing et al. 2006;Looper et al. 2008) offered the only opportunity to analyse the composition of silicates in brown dwarf atmospheres. The consensus picture from that sample is that the mid-infrared silicate absorption in L dwarfs is dominated by $\sim 0.1\text{--}1.0 \mu\text{m}$ amorphous enstatite or quartz grains that reside in optically thin cloud slabs near the top of the atmosphere, at temperatures of ~ 1100 K and pressures of $\lesssim 0.01$ bar (Burningham et al. 2021; Luna & Morley 2021, and references therein). This silicate cloud layer may overlay a deeper iron cloud deck (Burningham et al. 2021). A similar multi-layer scenario, comprising a patchy forsterite cloud above a deeper, optically thick iron deck, represents well the silicate absorption inferred in two young early-T dwarfs (Vos et al. 2022a).

The mid-infrared atmospheric modelling of silicates presented in Luna & Morley (2021) is the broadest to date. They model five of the six L3.5–L6 dwarfs with previously detected silicate absorption from Spitzer IRS. By virtue of the similarity in spectral types, the best-fit models in Luna & Morley (2021) all have similar fundamental parameters: four objects are inferred to have an effective temperature of $T_{\text{eff}} = 1800$ K and a surface gravity of $\log g = 5$ and one has $T_{\text{eff}} = 1700$ K and $\log g = 4$. The one object (2MASS J1507476–162738; L5) with a low-gravity best-fit model for the mid-infrared spectrum is unlikely to be young, however. It has no spectroscopic signatures of youth in $R\sim 900$ optical (Reid et al. 2000) or $R\sim 2000$ near-infrared (Rayner et al. 2009) spectra, and the BANYAN Σ algorithm yields a 99.9% probability of being an old field object. Filippazzo et al. (2015) find a semi-empirical surface gravity of $\log g = 5.18$, based on an assumed >500 Myr age and evolutionary models. As we have shown in Suárez et al. (2021), $R\sim 100$ Spitzer IRS spectra by themselves, as analysed in Luna & Morley (2021), may yield substantially less accurate results for effective temperature and surface gravity when fit by photospheric models compared to $R\sim 2300$ near-infrared spectra. Hence this object has a likely higher

gravity than inferred from the model best fit to the IRS spectrum in Luna & Morley (2021). Overall, the small number of previously known silicate-rich L-dwarf IRS spectra analysed in Luna & Morley (2021) and the similarity in effective temperatures and surface gravities, do not allow a differentiation among the mid-infrared silicate absorption feature as a function of fundamental parameters.

However, Luna & Morley (2021) do produce detailed predictions for the spectroscopic signatures of silicate condensates that can be compared to anticipated spectra from JWST. The recognition of a much larger sample of L dwarfs with detectable silicate absorption in Spitzer IRS spectra (Suárez & Metchev 2022), and the gravity-dependent sub-sampling that we have performed here, allow a first look at systematic effects as a function of surface gravity.

4.1 Dust Clouds in Young Atmospheres are Dominated by Heavier Grains

We use the Luna & Morley (2021) predictions to extract differences in silicate composition, grain size, or crystallinity that match the observed spectroscopic differences between low- and high-surface gravity mid-L dwarfs (Section 3). Specifically, we use the predictions for the mid-infrared silicate flux ratio F_{ratio} from Figure 7 in Luna & Morley (2021), wherein F_{ratio} is defined as the wavelength-dependent ratio of the grey-cloud (F_{grey}) to the condensate-cloud (F_{cloud}) model atmosphere. In so far as the grey-cloud model is representative of our featureless silicate-poor mid-L spectra, the Luna & Morley (2021) F_{ratio} metric is similar to the inverse of our continuum-divided spectra (Figure 4a). We plot this inverse in Figure 4b. The only difference is that in Luna & Morley (2021) the grey-cloud and condensate-cloud models are not scaled to each other in the silicate-free wavelength regions, while we have scaled both silicate-poor and silicate-rich mid-L spectra to the same average continuum (Figure 3).

A comparison between our Figure 4b and Figure 7 of Luna & Morley (2021) reveals that the redder and more rounded $9.5 \mu\text{m}$ silicate absorption profile in young low-gravity mid-L dwarfs is likely caused by $1 \mu\text{m}$ amorphous magnesium- and iron-bearing pyroxene ($\text{Mg}_x\text{Fe}_{1-x}\text{SiO}_3$) grains. Pyroxene is the only iron-bearing silicate modelled in Luna & Morley (2021) with a profile as asymmetric as the observed one, including a steeper slope over $8.0\text{--}9.5 \mu\text{m}$ and a flatter slope over $9.5\text{--}13 \mu\text{m}$. An admixture of larger ($>1 \mu\text{m}$) amorphous enstatite grains is also possible, given the inverse dependence of peak wavelength on dominant grain size (Luna & Morley 2021). However, the grains could not be as large as $10 \mu\text{m}$, as they would lack the characteristic absorption features and would instead behave as a source of grey opacity (Cushing et al. 2006; Luna & Morley 2021).

Conversely, the $\approx 9.1 \mu\text{m}$ peak and the narrower profile of silicate absorption in old high-gravity mid-L dwarfs points to the presence of $\lesssim 0.1 \mu\text{m}$ amorphous enstatite (MgSiO_3) or SiO grains. Figure 7 of Luna & Morley (2021) shows $0.1 \mu\text{m}$ amorphous enstatite grains peaking in absorption strength around $9.2 \mu\text{m}$ in a 1800 K atmosphere, vs. a peak at $9.4 \mu\text{m}$ for larger $1 \mu\text{m}$ grains. One-micron amorphous SiO grains exhibit a similar absorption peak and profile as $1 \mu\text{m}$ amorphous enstatite grains, and are also expected to peak closer to $9.1 \mu\text{m}$ if smaller in size. Contributions from other species are likely secondary. Thus, a contribution from amorphous or crystalline quartz (SiO_2), which peaks in strength at $\approx 8.8 \mu\text{m}$ is possible, but not likely, given the sharpness of the SiO_2 absorption feature (Luna & Morley 2021). A more accurate determination of the silicate and iron content and grain size of dust clouds in brown dwarf atmospheres awaits JWST MIRI observations, which will bring broader wavelength coverage at higher SNR and spectral resolution.

While the comparison to model predictions is not conclusive about the composition and size of the silicate grains in low- vs. high-gravity mid-*L* dwarfs, there is one consistent difference between the two. The types of grains that fit better the redder and broader silicate absorption observed in young low-gravity mid-*L* dwarfs are heavier than the grains that fit better the bluer and narrower silicate absorption profiles of old high-gravity mid-*L* dwarfs.

4.2 Lower-gravity Ultracool Atmospheres Have Lower Sedimentation Efficiency

The preceding spectroscopic analysis established that silicate grains in low-gravity atmospheres are both larger ($\sim 1 \mu\text{m}$) and composed of a heavier molecule ($\text{Mg}_x\text{Fe}_{1-x}\text{SiO}_3$) compared to silicates in high-gravity atmospheres, which have sizes of $\lesssim 0.1 \mu\text{m}$ and are dominated by MgSiO_3 or SiO . For example, for a typical $x = 0.4$ pyroxene ($\text{Mg}_{0.4}\text{Fe}_{0.6}\text{SiO}_3$) has a molecular weight of 23.9 g mol^{-1} per constituent atom, which is heavier than enstatite (MgSiO_3 , $20.1 \text{ g mol}^{-1} \text{ atom}^{-1}$) or SiO ($22.0 \text{ g mol}^{-1} \text{ atom}^{-1}$). Iron-rich pyroxene condensates are also more refractory than enstatite or SiO condensates, and so settle at lower altitudes in brown dwarf atmospheres (e.g., [Ackerman & Marley 2001](#); [Cooper et al. 2003](#); [Lodders 2003](#); [Woitke et al. 2020](#)). We have thus found spectroscopic evidence that the settling of dust condensates in ultracool atmospheres depends on surface gravity.

This confirms the very well-established theoretical expectation that low-gravity atmospheres have lower sedimentation efficiencies ([Ackerman & Marley 2001](#); [Cooper et al. 2003](#)), and that correspondingly the settling of dust clouds in low-gravity atmospheres happens at lower temperatures ([Stephens et al. 2009](#); [Madhusudhan et al. 2011](#); [Marley et al. 2012](#); [Charnay et al. 2018](#)), leading to dustier atmospheres in young objects.

Table 1. Sub-samples of mid-L dwarfs with silicate-rich and silicate-poor spectra.

Designation	Short Name	SpT _{opt}	Ref.	SpT _{IR}	Ref.	Silicate Index	ΔSi^a
Young silicate-rich mid-L spectra							
2MASS J03552337+1133437 ^b	0355+1133	L5 γ	Cruz et al. (2009)	L4 γ	Bardalez Gagliuffi et al. (2019)	1.29 \pm 0.02	0.19 \pm 0.02
2MASS J05012406–0010452 ^c	0501–0010	L4 γ	Cruz et al. (2009)	L4 γ	Gagné et al. (2015)	1.35 \pm 0.08	0.20 \pm 0.08
2MASS J14252798–3650229 ^b	1425–3650	L3	Reid et al. (2008)	L4 γ	Gagné et al. (2015)	1.32 \pm 0.04	0.20 \pm 0.04
2MASS J22443167+2043433 ^b	2244+2043	L6.5	Kirkpatrick et al. (2008)	L6–L8 γ	Gagné et al. (2015)	1.37 \pm 0.07	0.38 \pm 0.07
Old silicate-rich mid-L spectra							
2MASS J00043484–4044058	0004–4044	L5	Kirkpatrick et al. (2001)	L4.5	Knapp et al. (2004)	1.36 \pm 0.11	0.25 \pm 0.11
2MASS J01443536–0716142	0144–0716	L5	Liebert et al. (2003)	L5	Marocco et al. (2013)	1.29 \pm 0.05	0.18 \pm 0.05
2MASS J09201223+3517429 ^d	0920+3517	L6.5	Kirkpatrick et al. (2000)	T0p	Burgasser et al. (2006)	1.31 \pm 0.14	0.32 \pm 0.14
2MASS J12392727+5515371	1239+5515	L5	Kirkpatrick et al. (2000)	L5	Schneider et al. (2014)	1.48 \pm 0.12	0.37 \pm 0.12
2MASS J14482563+1031590	1448+1031	L4	Wilson et al. (2003)	L5.5	Schneider et al. (2014)	1.26 \pm 0.05	0.10 \pm 0.05
2MASS J17534518–6559559	1753–6559	L4	Reid et al. (2008)	L4	Marocco et al. (2013)	1.37 \pm 0.09	0.22 \pm 0.09
2MASS J18212815+1414010	1821+1414	L4.5	Looper et al. (2008)	L5p	Kirkpatrick et al. (2010)	1.25 \pm 0.01	0.11 \pm 0.01
2MASS J21481633+4003594	2148+4003	L6	Looper et al. (2008)	L6.5p	Kirkpatrick et al. (2010)	1.44 \pm 0.01	0.40 \pm 0.01
2MASS J22244381–0158521	2224–0158	L4.5	Kirkpatrick et al. (2000)	L3.5	Knapp et al. (2004)	1.38 \pm 0.06	0.24 \pm 0.06
Silicate-poor mid-L spectra							
2MASS J07003664+3157266	0700+3157	L3.5	Thorstensen & Kirkpatrick (2003)	1.02 \pm 0.04	–0.11 \pm 0.04
2MASS J09083803+5032088	0908+5032	L5	Cruz et al. (2003)	L9	Knapp et al. (2004)	0.89 \pm 0.04	–0.21 \pm 0.04
2MASS J10365305–3441380	1036–3441	L6	Gizis (2002)	L6.5	Burgasser et al. (2010)	0.83 \pm 0.05	–0.20 \pm 0.05
2MASS J11263991–5003550	1126–5003	L4.5	Burgasser et al. (2008)	L6.5p	Burgasser et al. (2008)	1.01 \pm 0.04	–0.13 \pm 0.04
2MASS J13314894–0116500	1331–0116	L6	Hawley et al. (2002)	L6	Marocco et al. (2015)	0.86 \pm 0.06	–0.18 \pm 0.06
2MASS J15150083+4847416	1515+4847	L6	Cruz et al. (2007)	L6.5	Cruz et al. (2003)	0.88 \pm 0.04	–0.15 \pm 0.04
2MASS J16262034+3925190	1626+3925	sdL4	Burgasser et al. (2007)	sdL	Burgasser (2004)	0.95 \pm 0.06	–0.20 \pm 0.06

^aSilicate index excess defined as the difference between the measured silicate index value for each dwarf and the median index for its spectral type (Section 2.1 and Figure 2a).

^bMember of the 110–150 Myr-old (Luhman et al. 2005; Barenfeld et al. 2013) AB Doradus moving group. References are Liu et al. (2013); Gagné et al. (2015); Vos et al. (2018) for 0355+1133, 1425–3650, and 2244+2043, respectively.

^cMember of either the Columba or Carina moving groups (Gagné et al. 2015), which are coeval groups at 20–40 Myr (Torres et al. 2008).

^dClose binary system with the individual components having near-infrared spectral types of L5.5 and L9 (Dupuy & Liu 2012). The binary is not resolved in the Spitzer observations and, therefore, the IRS spectrum is likely dominated by the brighter L5.5 dwarf.

5 CONCLUSION

We have established that the mid-infrared silicate absorption in the spectra of mid-*L* dwarfs is sensitive to surface gravity (Section 3). It is broader, redder, and more asymmetric for young $\log g \lesssim 4.5$ mid-*L* dwarfs than for their older $\log g \gtrsim 5.0$ counterparts. Comparisons to theoretical spectra reveal that the silicate grains in young mid-*L* dwarfs are heavier (Section 4.1). They are larger ($\sim 1 \mu\text{m}$) and dominated by silicates that are more refractory (magnesium- and iron-bearing pyroxene) than grains in the atmospheres of older mid-*L* dwarfs ($\lesssim 0.1 \mu\text{m}$ in size and dominated by enstatite or SiO). This result directly confirms that dust cloud sedimentation in low-gravity substellar atmospheres is suppressed (Section 4.2), as already anticipated by their redder optical and near-infrared photospheric colours (Kirkpatrick 2005; Filippazzo et al. 2015) and by their enhanced photometric variability (e.g., Metchev et al. 2015; Biller et al. 2015). The surface gravity dependence of the condensate physics and chemistry enhances the empirical context for JWST studies of brown dwarf and exoplanetary atmosphere.

ACKNOWLEDGEMENTS

We thank the referee Denise C. Stephens for a helpful report that significantly improved the quality of this paper. We thank Marina Gemma for discussions and suggestions on the use of appropriate nomenclature for dust grains. G.S. acknowledges support from NSF award #2009177. Support for this work was provided by the Canadian Space Agency under the Flights and Fieldwork for the Advancement of Science and Technology programme (reference no. 19FAWESB40). The spectra presented here are obtained entirely with the Spitzer Space Telescope, which was operated by the Jet Propulsion Laboratory, California Institute of Technology under a contract with NASA.

DATA AVAILABILITY

The spectra used in this analysis form part of the uniformly reprocessed set of Spitzer IRS spectra of 113 M5–T9 dwarfs published and available in Suárez & Metchev (2022) and on Genaro Suárez’ homepage¹.

REFERENCES

Ackerman A. S., Marley M. S., 2001, *ApJ*, **556**, 872
 Artigau É., Bouchard S., Doyon R., Lafrenière D., 2009, *ApJ*, **701**, 1534
 Bardalez Gagliuffi D. C., et al., 2019, *ApJ*, **883**, 205
 Barenfeld S. A., Bubar E. J., Mamajek E. E., Young P. A., 2013, *ApJ*, **766**, 6
 Biller B. A., et al., 2015, *ApJ*, **813**, L23
 Bowler B. P., Zhou Y., Morley C. V., Kataria T., Bryan M. L., Benneke B., Batygin K., 2020, *ApJ*, **893**, L30
 Burgasser A. J., 2004, *ApJ*, **614**, L73
 Burgasser A. J., Marley M. S., Ackerman A. S., Saumon D., Lodders K., Dahn C. C., Harris H. C., Kirkpatrick J. D., 2002, *ApJ*, **571**, L151
 Burgasser A. J., Geballe T. R., Leggett S. K., Kirkpatrick J. D., Golimowski D. A., 2006, *ApJ*, **637**, 1067
 Burgasser A. J., Cruz K. L., Kirkpatrick J. D., 2007, *ApJ*, **657**, 494
 Burgasser A. J.,Looper D. L., Kirkpatrick J. D., Cruz K. L., Swift B. J., 2008, *ApJ*, **674**, 451

Burgasser A. J., Cruz K. L., Cushing M., Gelino C. R.,Looper D. L., Faherty J. K., Kirkpatrick J. D., Reid I. N., 2010, *ApJ*, **710**, 1142
 Burningham B., et al., 2021, *MNRAS*, **506**, 1944
 Burrows A., et al., 1997, *ApJ*, **491**, 856
 Burrows A., Hubbard W. B., Lunine J. I., Liebert J., 2001, *Reviews of Modern Physics*, **73**, 719
 Charnay B., Bézard B., Baudino J. L., Bonnefoy M., Boccaletti A., Galicher R., 2018, *ApJ*, **854**, 172
 Cooper C. S., Sudarsky D., Milsom J. A., Lunine J. I., Burrows A., 2003, *ApJ*, **586**, 1320
 Cruz K. L., Reid I. N., Liebert J., Kirkpatrick J. D., Lowrance P. J., 2003, *AJ*, **126**, 2421
 Cruz K. L., et al., 2007, *AJ*, **133**, 439
 Cruz K. L., Kirkpatrick J. D., Burgasser A. J., 2009, *AJ*, **137**, 3345
 Cushing M. C., et al., 2006, *ApJ*, **648**, 614
 Cushing M. C., et al., 2008, *ApJ*, **678**, 1372
 Dupuy T. J., Liu M. C., 2012, *ApJS*, **201**, 19
 Dupuy T. J., Liu M. C., 2017, *ApJS*, **231**, 15
 Faherty J. K., et al., 2016, *ApJS*, **225**, 10
 Filippazzo J. C., Rice E. L., Faherty J., Cruz K. L., Van Gordon M. M.,Looper D. L., 2015, *ApJ*, **810**, 158
 Gagné J., et al., 2015, *ApJS*, **219**, 33
 Gagné J., et al., 2018, *ApJ*, **856**, 23
 Gizis J. E., 2002, *ApJ*, **575**, 484
 Hawley S. L., et al., 2002, *AJ*, **123**, 3409
 Houck J. R., et al., 2004, *ApJS*, **154**, 18
 Kirkpatrick J. D., 2005, *ARA&A*, **43**, 195
 Kirkpatrick J. D., et al., 2000, *AJ*, **120**, 447
 Kirkpatrick J. D., Dahn C. C., Monet D. G., Reid I. N., Gizis J. E., Liebert J., Burgasser A. J., 2001, *AJ*, **121**, 3235
 Kirkpatrick J. D., Barman T. S., Burgasser A. J., McGovern M. R., McLean I. S., Tinney C. G., Lowrance P. J., 2006, *ApJ*, **639**, 1120
 Kirkpatrick J. D., et al., 2008, *ApJ*, **689**, 1295
 Kirkpatrick J. D., et al., 2010, *ApJS*, **190**, 100
 Knapp G. R., et al., 2004, *AJ*, **127**, 3553
 Liebert J., Kirkpatrick J. D., Cruz K. L., Reid I. N., Burgasser A., Tinney C. G., Gizis J. E., 2003, *AJ*, **125**, 343
 Liu M. C., Dupuy T. J., Allers K. N., 2013, *Astronomische Nachrichten*, **334**, 85
 Lodders K., 2002, *ApJ*, **577**, 974
 Lodders K., 2003, *ApJ*, **591**, 1220
 Looper D. L., et al., 2008, *ApJ*, **686**, 528
 Luhman K. L., Stauffer J. R., Mamajek E. E., 2005, *ApJ*, **628**, L69
 Luna J. L., Morley C. V., 2021, *ApJ*, **920**, 146
 Madhusudhan N., Burrows A., Currie T., 2011, *ApJ*, **737**, 34
 Marley M. S., Saumon D., Cushing M., Ackerman A. S., Fortney J. J., Freedman R., 2012, *ApJ*, **754**, 135
 Marocco F., et al., 2013, *AJ*, **146**, 161
 Marocco F., et al., 2015, *MNRAS*, **449**, 3651
 Metchev S. A., et al., 2015, *ApJ*, **799**, 154
 Miles B. E., et al., 2022, arXiv e-prints, p. arXiv:2209.00620
 Rayner J. T., Cushing M. C., Vacca W. D., 2009, *ApJS*, **185**, 289
 Reid I. N., Kirkpatrick J. D., Gizis J. E., Dahn C. C., Monet D. G., Williams R. J., Liebert J., Burgasser A. J., 2000, *AJ*, **119**, 369
 Reid I. N., Cruz K. L., Kirkpatrick J. D., Allen P. R., Mungall F., Liebert J., Lowrance P., Sweet A., 2008, *AJ*, **136**, 1290
 Roellig T. L., et al., 2004, *ApJS*, **154**, 418
 Schneider A. C., Cushing M. C., Kirkpatrick J. D., Mace G. N., Gelino C. R., Faherty J. K., Fajardo-Acosta S., Sheppard S. S., 2014, *AJ*, **147**, 34
 Stephens D. C., et al., 2009, *ApJ*, **702**, 154
 Suárez G., Metchev S., 2022, *MNRAS*, **513**, 5701
 Suárez G., Metchev S., Leggett S. K., Saumon D., Marley M. S., 2021, *ApJ*, **920**, 99
 Thorstensen J. R., Kirkpatrick J. D., 2003, *PASP*, **115**, 1207
 Torres C. A. O., Quast G. R., Melo C. H. F., Sterzik M. F., 2008, in Reipurth B., ed., , Vol. 5, Handbook of Star Forming Regions, Volume II. p. 757
 Vos J. M., Allers K. N., Biller B. A., Liu M. C., Dupuy T. J., Gallimore J. F., Adenuga I. J., Best W. M. J., 2018, *MNRAS*, **474**, 1041

¹ <https://gsuarezcastro.wixsite.com/gsuarez/research>

- Vos J. M., et al., 2019, *MNRAS*, **483**, 480
- Vos J. M., et al., 2022a, arXiv e-prints, p. [arXiv:2212.07399](#)
- Vos J. M., Faherty J. K., Gagné J., Marley M., Metchev S., Gizis J., Rice E. L., Cruz K., 2022b, *ApJ*, **924**, 68
- Wilson J. C., Miller N. A., Gizis J. E., Skrutskie M. F., Houck J. R., Kirkpatrick J. D., Burgasser A. J., Monet D. G., 2003, in Martín E., ed., IAU Symposium Vol. 211, Brown Dwarfs. p. 197
- Woitke P., Helling C., Gunn O., 2020, *A&A*, **634**, A23
- Zuckerman B., 2019, *ApJ*, **870**, 27

This paper has been typeset from a \LaTeX file prepared by the author.